Title

Septins modulate the autophagy response after nutrient starvation.

Journal

Molecular Biology of the Cell, 35(1)

Authors

Perucho-Jaimes, Luis

Do, Jonathan

Van Elgort, Alexandria

et al.

Publication Date

2024

DOI

10.1091/mbc.E22-11-0520

Peer reviewed

Septins modulate the autophagy response after nutrient starvation

Luis Perucho-Jaimes†, Jonathan Do†, Alexandria Van Elgort, and Kenneth B. Kaplan*
Department of Molecular and Cellular Biology, University of California, Davis, Davis, CA 95616

ABSTRACT **The pathways that induce macroautophagy (referred to as autophagy hereafter) in response to the stress of starvation are well conserved and essential under nutrient-limiting conditions. However, less is understood about the mechanisms that modulate the autophagy response. Here we present evidence that after induction of autophagy in budding yeast septin filaments rapidly assemble into discrete patches distributed along the cell cortex. These patches gradually mature over 12 h of nutrient deprivation to form extended structures around Atg9 membranes tethered at the cortical endoplasmic reticulum, a class of membranes that are limiting for autophagosome biogenesis. Loss of cortical septin structures alters the kinetics of autophagy activation and most dramatically extends the duration of the autophagy response. In wild-type cells, diffusion of Atg9 membranes at the cell cortex undergoes transient pauses that are dependent on septins, and septins at the bud neck block the diffusion of Atg9 membranes between mother and daughter cells. We conclude that septins reorganize at the cell cortex during autophagy to locally limit access of Atg9 membranes to autophagosome assembly sites, and thus modulate the autophagy response during nutrient deprivation.**

SIGNIFICANCE STATEMENT

- The pathways that ensure the proper activation and then down regulation of macroautophagy are not well understood. Here we provide evidence that septin filaments reorganize at the cell cortex during nutrient deprivation to limit the autophagy response.
- We provide data to support the model that septins limit the diffusion of membranes at the cell cortex necessary for formation of autophagosomes.
- This suggests a novel mechanism to consider when studying normal or disease state autophagy responses.

Monitoring Editor
Amy Gladfelter
University of North Carolina, Chapel Hill

Received: Nov 18, 2022
Revised: Sep 19, 2023
Accepted: Oct 16, 2023

This article was published online ahead of print in MBoC in Press (http://www.molbiolcell.org/cgi/doi/10.1091/mbc.E22-11-0520) on November 1, 2023.

†These authors contributed equally to the work

*Address correspondence to: Kenneth B. Kaplan (kbkaplan@ucdavis.edu).

Abbreviations used: BFP, blue fluorescent protein; dsRed, discosoma red fluorescent protein; ER, endoplasmic reticulum; ERES, endoplasmic reticulum exit sites; GFP, green fluorescent protein; PAS, phagophore assembly site; YPD, yeast extract peptone dextrose.

INTRODUCTION

Macroautophagy (hereafter referred to as autophagy) is a conserved process in eukaryotes that is active at a basal level to maintain organelle homeostasis and then increases in response cell stresses such as nutrient deprivation, a condition that leads to the induction of bulk, nonselective autophagy and nutrient recycling. Targeted loss of autophagy in mouse models results in accumulation of aberrant organelles and in yeast autophagy becomes essential under nutrient deprivation conditions (Tsukada and Ohsumi, 1993; Klionsky *et al*., 2003; Komatsu *et al*., 2005). In both basal and bulk autophagy, careful modulation of pathway activation and, due to the degradative nature of autophagy, downregulation is necessary

to avoid inappropriate destruction of organelles and cytoplasm. Failure to properly modulate the autophagy response can contribute to cellular disease states, for example, by allowing cancer cells to survive starvation conditions or failing to clear the accumulation of aberrant protein aggregates in neurodegenerative disease (Mizushima *et al.*, 2008; Meng *et al.*, 2019; Chen and Gibson, 2021).

The steps associated with the initiation of autophagy and the formation of autophagosomes have been described in detail in budding yeast: initiation is accompanied by the nucleation of a multiprotein complex that forms the phagophore (a disk-like, membrane structure that forms around cargo) assembly site (PAS), that recruits lipids that form the double membrane autophagosome around cargo, and culminates with the fusion of the autophagosome with the vacuole, cargo degradation and efflux of breakdown products into the cytosol (for review, Delorme-Axford and Klionsky, 2018). Under nutrient-rich conditions, a series of upstream kinases (Tor, PKA, and Snf1) integrate signals from nutrient sensors to inhibit the Atg1 kinase by phosphorylating and activating the Atg1 inhibitor subunit, Atg13 (Noda and Ohsumi, 1998; Cebollero and Reggiori, 2009). Under nutrient deprivation, dephosphorylation of Atg13 is favored, allowing Atg1 activation and the initiation of PAS assembly. Under these conditions, a large array of proteins are recruited to PAS and a partial list includes: Atg9, the only autophagy-specific integral membrane protein, which is trafficked from cortical ER exit sites (ERES) and is required to transfer lipids to the growing phagophore (Matoba *et al.*, 2020; Orii *et al.*, 2021); the E1-like enzyme, Atg7, which mediates the conjugation of Atg12 to Atg5 and converts nonlipidated Atg8 to its phosphatidylethanolamine-conjugated form that interacts with the growing phagophore and is ultimately transported into the vacuole in the final steps of membrane fusion (for full review of the steps, see Feng *et al.*, 2014). In principle, regulation of upstream inhibitory kinases or activating phosphatases creates a plausible mechanism to modulate the levels of autophagy under a variety of conditions. However, studies on the repression of ATG gene transcription, suggest a more complex and integrated regulatory circuit is involved.

Autophagy has been primarily studied under nutrient starvation conditions, or after rapamycin treatment, both of which globally inhibits the Tor kinase and result in the initiation of bulk, nonselective autophagy. The formation of PAS and trafficking to the vacuole occurs within minutes of nutrient deprivation or rapamycin treatment and can last for hours if these conditions are maintained. Though a great deal is known about induction of autophagy under these conditions, less is known the mechanisms that modulate the extent of pathway activation and the kinetics of downregulation. Under nutrient-rich conditions, a series of transcriptional repressor complexes keeps autophagy at basal levels, and these repressors are themselves inhibited by nutrient deprivation (for review, Delorme-Axford and Klionsky, 2018). For example, the histone deacetylase complex, Rpd3, is targeted to and represses transcription at several ATG gene promotors, including *ATG8* and *ATG9*. The Ume6 subunit targets the complex to the *ATG8* promoter and loss of *UME6* leads to elevated levels of Atg8 and an increase autophagosome size but does not increase the frequency of autophagosome formation (Xie *et al.*, 2008). The Pho23 subunit of the Rpd3 complex is required to target and repress *ATG9* transcription under nutrient-rich conditions. Activation of autophagy derepresses *ATG9* transcription, which increases the frequency of autophagosome formation (Jin *et al.*, 2014), probably by increasing the rate of lipid transfer to growing phagophores. Atg9 and its associated lipid transfer activity are also regulated at the level of vesicular trafficking between ERES, the growing phagophore and retrograde trafficking back to ER membrane sites (Reggiori *et al.*, 2004; Graef *et al.*, 2013). Thus, fine tuning of autophagy can occur through regulation of gene transcription or vesicular trafficking, or both. In principle, similar repressive mechanisms might also be involved in the downregulation of autophagy after prolonged nutrient deprivation, but this has not be studied in detail.

The fine tuning of autophagy, especially in response to cell stress, is implicated in protection from disease and there are numerous examples of its dysregulation in disease states, including cancer and neurodegenerative disease (Mizushima *et al.*, 2008; Lei and Klionsky, 2021). A number of studies have implicated septins in modulating the autophagy response. For example, septins have been shown to form cages around nonmotile *Listeria monocytogenes* and *Shigella flexneri* and evidence suggests an interdependence between septin cage formation and the recruitment of autophagy proteins to target these intracellular bacteria to lysosomes (for review, Robertin and Mostowy, 2020). Paradoxically, septins and the p62 autophagy receptor have been shown to be required to maintain *Shigella flexneri* in a metabolically active state, possibly by allowing intracellular pathogens to exploit autophagy to increase nutrient access and thus proliferation (Lobato-Márquez *et al.*, 2019). In budding yeast, septins have been more directly implicated in autophagy, where they have been shown to associate with PAS as well as cortical membranes during starvation and have been reported to be required for normal autophagosome biogenesis (Barve *et al.*, 2018a, 2018b). However, their precise role at the cell cortex or at PAS and how they regulate autophagosome formation remains uncertain.

Septin filaments interact with negatively charged lipids typically associated with plasma membranes and primarily assemble from octamers composed of tetramer building blocks (Woods and Gladfelter, 2021). Septins have been generally implicated in establishing cell asymmetries or specialized cellular subdomains (McMurray and Thorner, 2009; Spiliotis and Gladfelter, 2012; Marquardt *et al.*, 2021; Russo and Krauss, 2021). Mechanistically, evidence supports septin filaments acting both as scaffolds for assembling large protein complexes as well as diffusion barriers that may work by partitioning the cortical endoplasmic reticulum (ER) at the bud neck, strongly restricting the free diffusion of integral membrane proteins embedded in the cortical ER and associated with plasma membrane contact sites (Takizawa *et al.*, 2000; Seshan *et al.*, 2002; Luedeke *et al.*, 2005; Chao *et al.*, 2014; Sugiyama and Tanaka, 2019). Septins are primarily observed at the mother-bud neck in budding yeast where they are important for polarized cell growth and cytokinesis. Despite their enrichment at the mother-bud neck, there are likely multiple pathways that regulate their organization. They disassemble during mitotic exit and ER stress induces changes in septin organization that prevents cell-cycle reentry (Babour *et al.*, 2010; Chao *et al.*, 2019), implicating cell stress pathways in septin regulation. The change in septin organization during autophagy raises the possibility that septins act to organize specific membrane subdomains related to autophagy and in response nutrient stress. To explore this possibility in more detail, we used high-resolution fluorescent microscopy to characterize the changes in septins during the induction, amplification, and downregulation of autophagy.

RESULTS

Septins primarily found in cortical "patches" after induction of autophagy

To understand how septins respond to and regulate autophagy during nutrient deprivation, we used spinning disk confocal fluorescent microscopy followed by image deconvolution to enhance resolution of septin structures (see *Materials and Methods*). Under nutrient

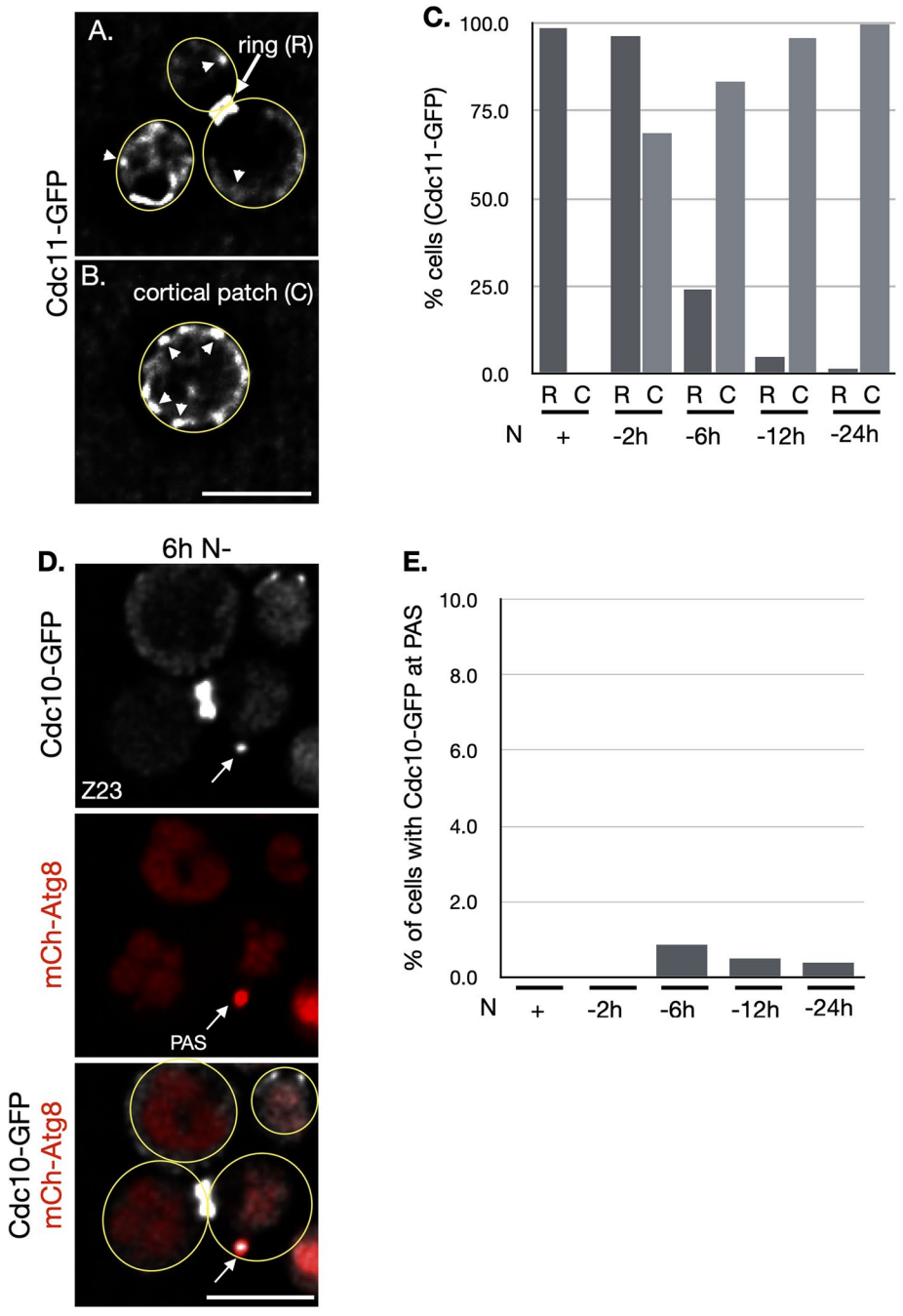

FIGURE 1: Septins form cortical patches during nutrient-deprivation. Cells expressing septin subunit GFP fusions were imaged after switching from complete medium to nutrient-limiting medium and processed as described in *Materials and Methods*. (A) A cell expressing Cdc10-GFP after 2 h nutrient-deprivation; arrow indicates a septin ring (R) at the bud neck and arrowheads indicate low-intensity cortical septin patches. (B) A cell after 6 h of nutrient-deprivation; arrowheads indicate high-intensity cortical septin patches. (C) Septin organization was classified in cells under the indicated growth conditions as "rings" (at the bud neck) or cortical patches ($n > 150$ cells for each time point). (D) Cells expressing Cdc10-GFP and mCh-Atg8 were imaged after 6 h of nutrient-deprivation and an example image of a cell with Cdc10-GFP overlapping with an mCh-Atg8 PAS structure (arrow). (E) Septin localization at PAS was quantified as a percentage of cells ($n > 150$ cells) at the indicated time points after nutrient deprivation (N-). Circles in images represent the cell outline from unprocessed images. Scale bars = 5 μm.

deprivation conditions, we observed the appearance of smaller assemblies of septins distributed along the cell cortex that we will refer to as cortical septin patches. These structures are reminiscent of previously described cortical membrane localization of septins under starvation conditions (Barve. Current Genetics. 2018). Protein fusions to multiple septin subunits revealed similar cortical patch structures and using pairwise fusions to distinct septin proteins, we show that multiple septin subunits are present in the same patches at the same time (Figure 1A; Supplemental Figure S1, A and B). After 2 h of nutrient deprivation, the majority of cells still maintain septin filaments organized as collars or rings at the bud neck (Figure 1, A and C; Supplemental Figure S1, A and B), although low intensity cortical patches were observed in the majority of these same cells (Figure 1A; see arrowheads). The fraction of cells with septins assembled at the bud neck dramatically decreases at 6 h and are almost completely absent by 12 h of nutrient deprivation (Figure 1, B and C). As septin filaments at the bud neck disassemble, the intensity of septins in cortical patches increases along with the number of cells with cortical septin patches (Figure 1C). The kinetics of cortical patch formation suggest that these assemblies are not dependent on disassembly of bud neck septin filaments, though we cannot exclude the possibility that septin subunits from the bud neck contribute to the final maturation of cortical patches. As previously reported (Barve *et al.*, 2018b), we observe septin subunits colocalized with PAS (as visualized with an Atg8 fluorescent protein fusion) but only in a small percentage of cells under nutrient deprivation (Figure 1, D and E; Supplemental Figure S1, C and F). We conclude that the primary change to septins during nutrient deprivation is their assembly into cortically distributed patches that mature over time.

To further characterize septin filaments at the cell cortex, we imaged cells coexpressing a septin subunit fusion, Cdc10-GFP, an ER marker (HDEL-dsRed) and a vacuolar marker (BFP-Pho8). As expected, septins form collars or rings between mother and daughter cells in vegetatively growing cells (i.e., nutrient-rich conditions), positioned at the plasma membrane, distal to the cortical ER and the internally positioned vacuole(s) (Figure 2, A-C). A volume projection and rotation around the X axis demonstrates septin rings at a position consistent with the proposed role of septins in partitioning cortical ER membranes between mother and daughter cells (Figure 2, D and E; Luedeke*et al.*, 2005; Sugiyama and Tanaka, 2019). Autophagy was induced for 12 h using rapamycin at which time the majority of cells display septin patches distributed along the cell cortex (Figures 2F). Septin patches were observed to

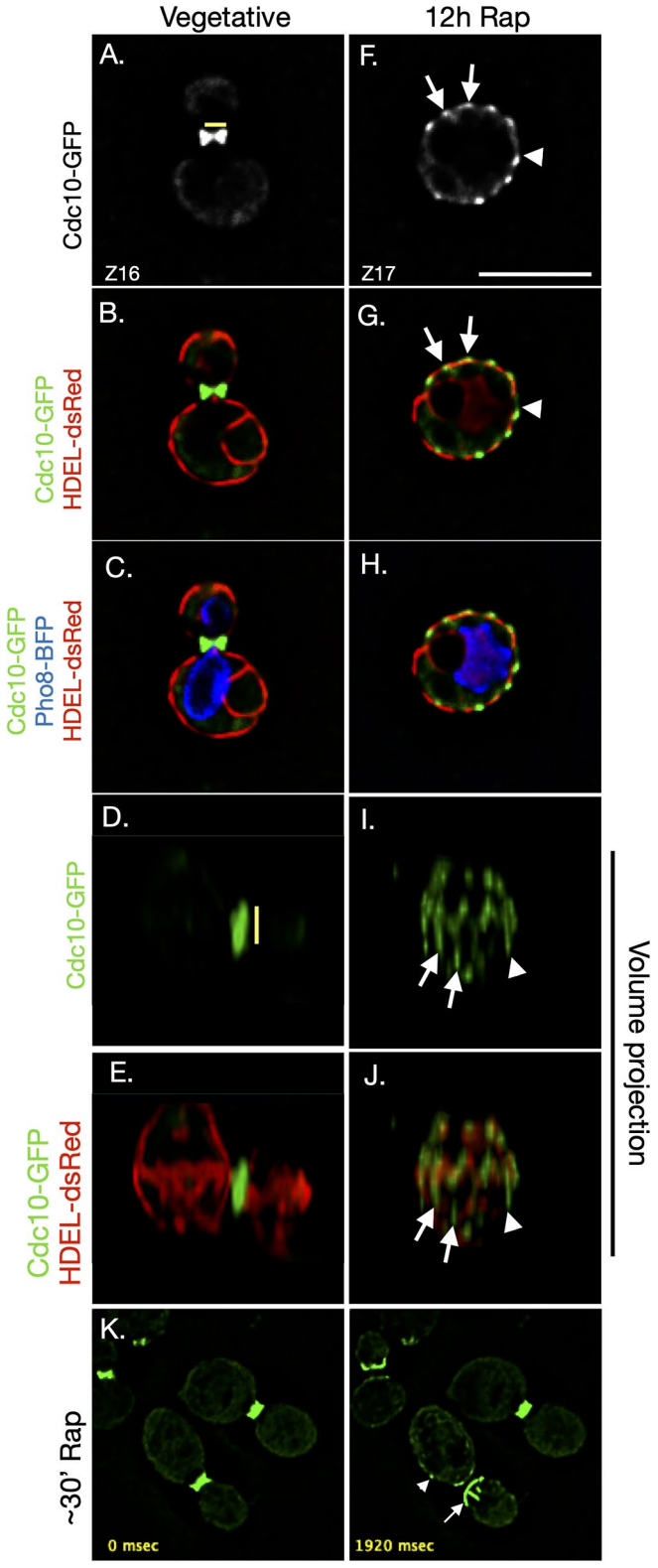

FIGURE 2: Septin cortical patches form "bars" that interdigitate with ER membranes after rapamycin treatment. Images were collected from cells growing in nutrient-rich medium (vegetative) or after treatment with rapamycin for 12 h and processed as described in *Materials and Methods*. (A) An example of Cdc10-GFP (gray) localization in a medium-budded cell (yellow line indicates the division plane) from a single Z-slice in the middle of the cell. (B) The same cell shown with an overlay of Cdc10-GFP (green) and HDEL-dsRed (red; to mark the ER) and in (C) an overlay of the same cell that includes BFP-Pho8 (blue; to mark the vacuole). A projected volume of the same cell was rotated 90 degrees to the right and then around the X axis to show (D) septins (Cdc10-GFP, green) and septins overlaid with (E) HDEL-dsRed (yellow line indicates division plane). (F–J) An example of a cell with images organized as in (A–E) but 12 h after rapamycin treatment and the volume projection only rotated around the X axis. Arrows and arrowhead indicate the cortical patches in a single Z (F and G) and the fluorescence signal in the projected volume after rotation (I and J). (K) Selected time-lapse images from movie 2 (Supplemental Movie 2; Supplemental Figure S2A; the 0 m/s time stamps is the first frame of the movie) that was created from a maximum Z projection; time-lapse images were collected ~30 min after rapamycin treatment. The arrow indicates septin ring reoriented and migrating along the cell cortex. The arrowheads indicate a low intensity cortical septin patch.

assemble at a position consistent with their interaction with plasma membranes, distal to the cortical ER and distinct from the vacuole (Figure 2, F–H; white arrows). A volume projection shows that cortical septin patches vary in size from discrete ~0.5-µm patches to bar-like structures that extend up to 4 µm (see arrows and the arrowhead, Figure 2, I and J). The septin bar-like structures are interspersed with morphologically similar cortical ER structures, suggesting that septins form multiple; discrete interfaces between the plasma membrane and cortical ER membranes after the induction of autophagy (Figure 2J).

To characterize the kinetics of septin patch formation during autophagy induction, we collected time series from cells expressing Cdc10-GFP immediately after treatment with rapamycin. We observed a sudden dramatic reorganization of septins that coincided with the initiation of septin ring separation (when the spacing between rings is >500 nm) during mitotic exit (Figure 2K; Supplemental Figure 2A; Supplemental Movie 2). In time-lapse movie 2, the mother cell septin ring disassembles within a single time frame (240 ms; from 720–960 ms time frames, Supplemental Figure S2A) after septin rings at the bud neck reach their maximal thickness. In the same time increment, the septin ring on the daughter cell side reorients to form perpendicular bars that migrate down the cortex of the daughter cell. Shortly after (<1 s), brighter septin patches are visible at the cortex of both the mother and daughter cell (see arrows in Supplemental Figure S2A). In cells with septin rings at the bud neck that have not yet exited mitosis, few detectable changes in septin organization were observed during duration of the movie (80 min total; e.g., the cell in the upper right of movie 1; septin rings <350 nm separated). Although low intensity septin patches form rapidly, they did not reach their maximal size and intensity until between 12 and 24 h after rapamycin treatment (Supplemental Figure S2B). The persistence of cortical septin patches for long periods after induction of autophagy raised the possibility that these patches, once formed, are stable. To measure their stability, we used lattice lightsheet fluorescence microscopy to rapidly acquire images (10 s/frame) with minimal photodamage. We observed that septin patches at the cell cortex are stable in their relative positioning and in their overall intensities for over 500 s (see Supplemental Movie 3, images from the time sequence and kymograph analyses, Supplemental Figure S2, F-H). Together, these results argue that formation of cortical septin patches occurs rapidly after induction of autophagy but following the exit from mitosis, after which patches gradually mature into stable structures.

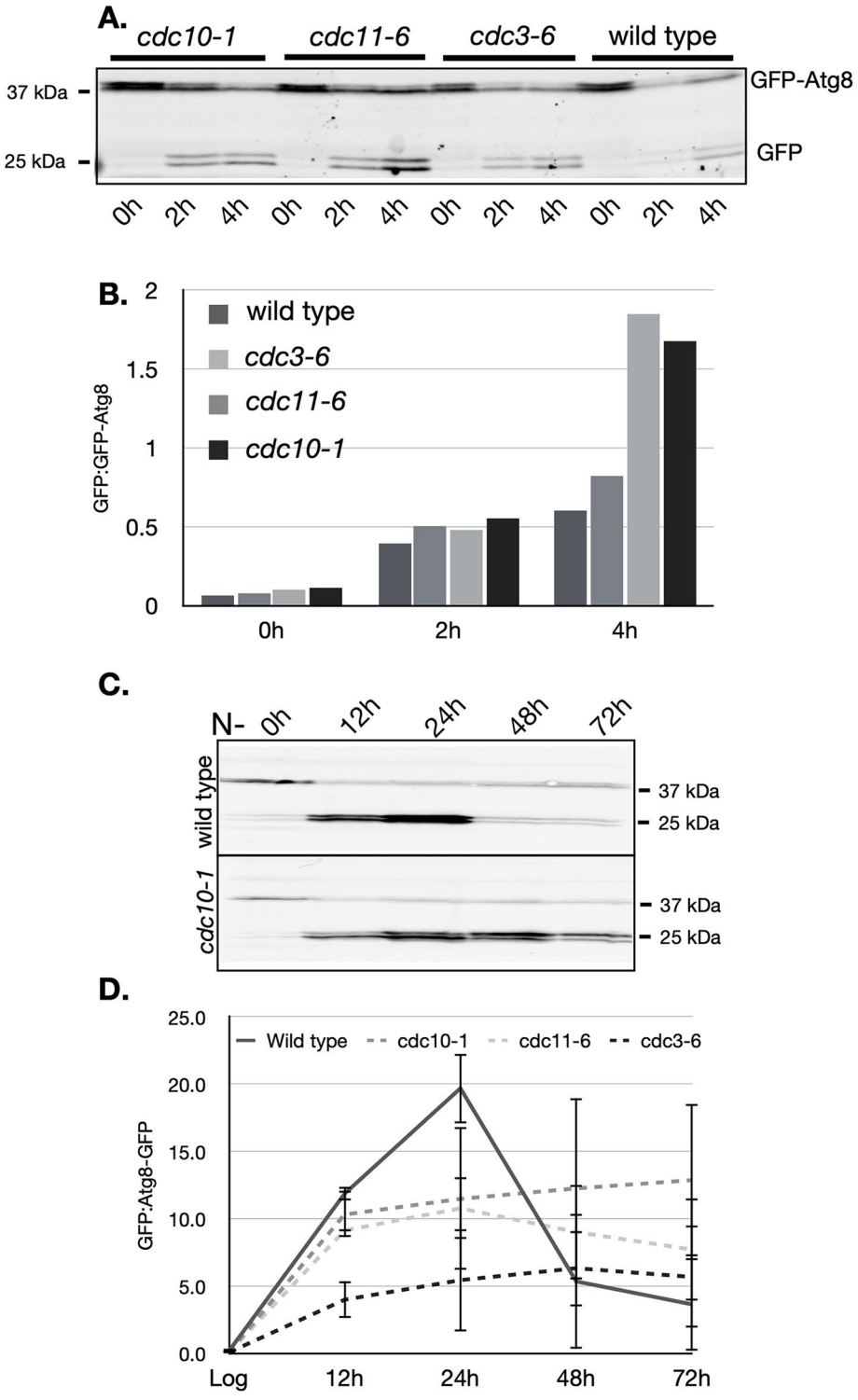

FIGURE 3: Kinetics of autophagic flux after nutrient deprivation in wild-type and septin mutants. (A) Wild-type, *cdc10-1*, *cdc11-6*, or *cdc3-6* cells were grown to log phase at 25°C and then shifted to nutrient-limiting medium and 37°C for 2 and 4 h. Cells were harvested and proteins extracted for Western blot analysis using an anti-GFP antibody. (B) The GFP fragment and full-length GFP-Atg8 were quantified and expressed as a ratio (GFP:GFP-Atg8). (C) Western blot of autophagic flux from wild-type and *cdc10-1* cells grown to log phase and then shifted to nutrient-limiting medium and 30°C for the indicated times and analyzed by Western blot. (D) GFP:GFP-Atg8 ratios were determined by quantifying Western blot signals from three separate experiments using wild-type, *cdc10-1*, *cdc11-6*, and *cdc3-6* cells. Error bars represent SD between experiments.

Septins are required for proper downregulation of autophagic flux

To assess the role of cortical septin patches during autophagy, we measured autophagic flux in wild-type cells and in cells with conditional septin alleles. We used a GFP-Atg8 fusion expressed under its native promoter to quantify flux based on the appearance of a stable GFP fragment that forms after trafficking of autophagosomes to the vacuole (Klionsky *et al.*, 2021). We grew cells to log phase at permissive temperature, shifted to nonpermissive conditions (37°C) at the same time nutrients were withdrawn and monitored flux at 2 and 4 h. The ratio of GFP to GFP-Atg8 was similar before starvation (Figure 3A, 0 h) and increased as expected in wild type and to similar levels in the three septin alleles we examined at 2 h of nutrient deprivation. After 4 h, flux levels are equal to (for *cdc11-6*) or higher (for *cdc10-1* and *cdc3-6*) in septin mutants compared with wild-type cells (Figure 3, A and B). These results argue that septins are not required for the induction of autophagy and suggest that instead they could serve a role in limiting autophagy.

As we observed septin patches mature late in the autophagy response, we next examined how loss of septins affects autophagic flux at starvation time points coincident with septin patch maturation. In these experiments, we grew cells in starvation medium at 30°C, a condition that prevents septin assembly without significant increases in failed cytokineses or abnormal bud morphologies before cells arresting in G1 (see Supplemental Figure S3A). In wild-type cells, autophagic flux peaks at 24 h after nutrient deprivation, decreases dramatically at 48 h and slowly decreases after (Figure 3, C and D). In contrast, the three septin alleles examined all exhibit persistent autophagic flux after 24 h (Figure 3, C and D). When normalized to vegetatively growing cells, septin mutants exhibit 3.2 to 6.8-fold more flux than wild-type cells at 72 h after nutrient deprivation (see Supplemental Figure S3B). The levels of GFP-Atg8 are similar under nutrient-rich conditions and increase to similar extents after nutrient deprivation in wild-type and septin mutants, arguing against an increase in GFP-Atg8 levels in septin mutants (see Supplemental Figure S3, C–E). We interpret these results to suggest that septin patches at the cell cortex form to limit autophagy especially after prolonged nutrient starvation.

The persistence in flux in septin mutants might be explained by changes in any one of the steps in autophagosome biogenesis

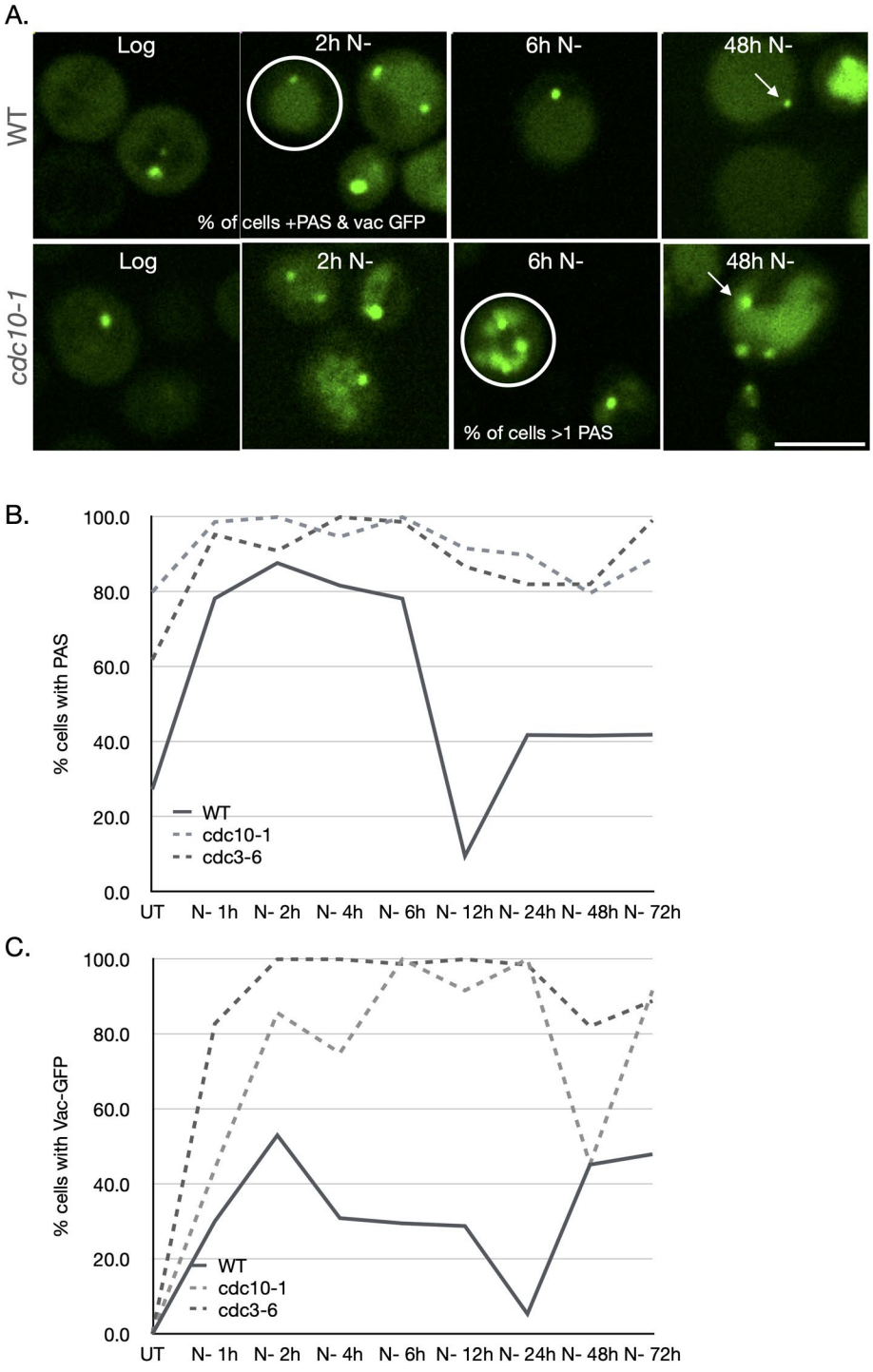

FIGURE 4: Quantification of GFP-Atg8 in PAS formation and vacuolar trafficking in wild-type and septin mutants after nutrient deprivation. (A) Representative images of wild-type (WT) or *cdc10-1* cells expressing GFP-Atg8 from its native promoter in vegetatively grown cells (log) and after nutrient deprivation for the indicated times. The labeled circles highlight the categories of GFP-Atg8 localization that were quantified: percentage of cells with PAS and vacuolar GFP; percentage of cells with more than one PAS (Supplemental Figure S4A). The arrows highlight the different size PAS that form at late time points in wild-type and *cdc10-1*. (B) The percentage of cells with GFP-Atg8 labeled PAS was quantified for wild-type, *cdc3-6* and *cdc10-1* cells grown in nutrient-rich medium or under nutrient deprivation conditions for the times indicated (100–150 cells counted for each time point). (C) The percentage of cells vacuolar GFP signal as a sign of flux (see text) as quantified in (B). Vacuolar staining provided in Supplemental Figure S3. Scale bar = 5 μm

and trafficking. To gain more insight into which steps are regulated by septins, we analyzed individual cells expressing GFP-Atg8 by spinning disk confocal microscopy. We quantified the percentage of cells with PAS, with more than one PAS and with vacuolar GFP signal (see examples in Figure 4A and vacuolar staining panels in supplemental Figure S3G and S3H). In wild-type cells grown at 30°C, the percentage of cells with at least one PAS increased after shifting cells to nutrient starvation conditions representing the rapid induction of autophagy (peaking at 2 h; Figure 4B); consistent with the flux analysis, the percentage of cells with PAS dropped dramatically 12 h later. The PAS that were observed at later time points (after 24 h) were typically reduced in intensity and never reached the frequencies observed immediately after autophagy induction (Figure 4A, arrow in WT 48 h N- and Figure 4B). In contrast, both *cdc10-1* and *cdc3-6* exhibited persistent formation of PAS with high intensity GFP-Atg8 signal for 72 h after nutrient deprivation (Figure 4, A, arrow in *cdc10-1* 48 h N-, and B). The number of cells with more than one PAS peaks in wild-type cells shortly after induction (between 2 and 4 h), and while a similar kinetic peak occurs in septin mutants, the initial increase is slightly more rapid than wild-type cells and persists longer (see Supplemental Figure S3F). The presence of GFP in vacuoles also persists in septin mutants, which supports the argument that the sustained formation of PAS in septin mutants functionally contributes to autophagy (see Figure 4, A and C; Supplemental Figure S3, G and H). Though our data suggest septins have a modest impact on limiting PAS formation early in autophagy induction (see Figure 3, A and B, see *Discussion*), their impact on autophagy is most dramatically observed in limiting PAS formation during extended periods of starvation (i.e., after 12 h). Consistent with their role in limiting autophagy, we find that septin mutants do not contribute to loss of cell viability or an increase in cell death under nutrient deprivation conditions, as observed for mutations in genes required for the induction of autophagy (see Supplemental Figure S4, A–C).

Septins are positioned near and limit Atg9 membranes

The reported position of septin patches at the cell cortex near Atg9 membranes and the contribution of cortical Atg9 membranes to autophagosome biogenesis (Noda *et al.*, 2000) led us to examine the relationship

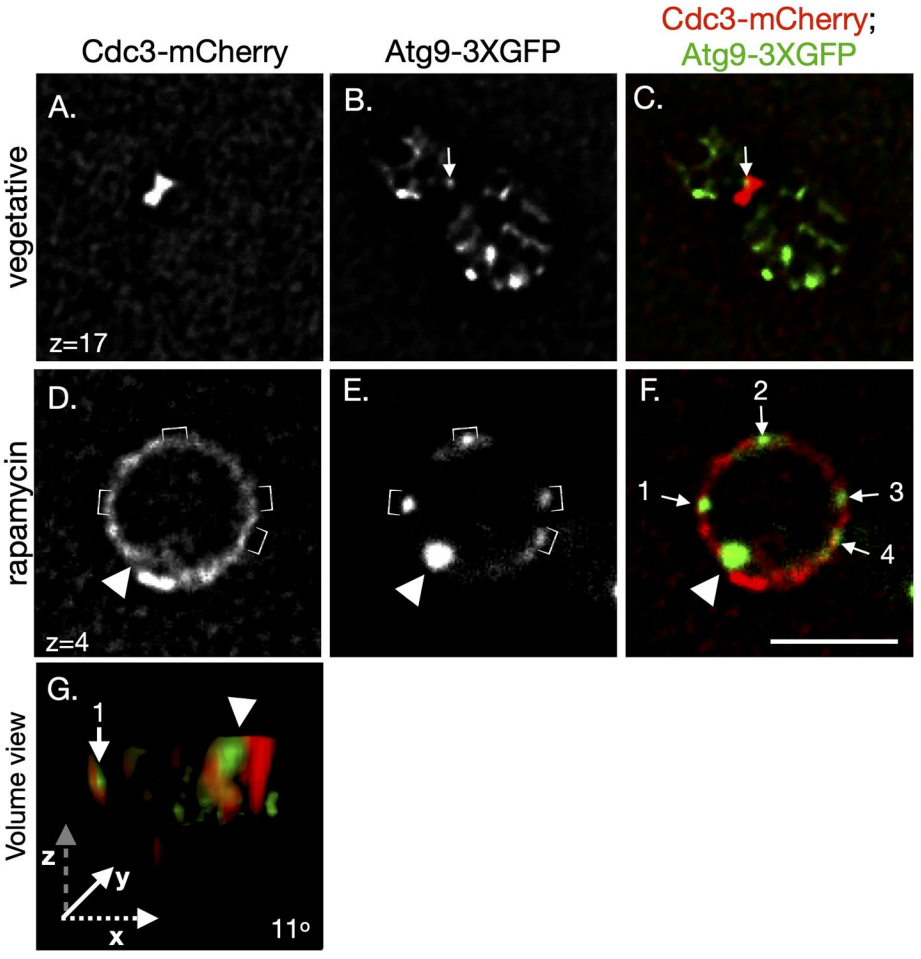

FIGURE 5: Juxtaposition of cortical septin patches and Atg9 membranes tethered to the ER cortex. Cells coexpressing Cdc3-mCherry (Cdc3-mCh [red]) and Atg9-3XGFP (green) were grown vegetatively and a single Z-slice through the middle of the cell is presented to show (A) Cdc3-mCh at the bud neck, (B) Atg9-3XGFP positioned at cortical and internal ER membrane tubules, and (C) an overlay of Cdc3-mCh (red) and Atg9-3XGFP (green; arrow indicates an Atg9-3XGFP vesicle localized near the bud neck septins). The same strain was treated with rapamycin for 6 h and images are presented as above. (D) A single Z-slice through the middle of the cell highlights Cdc3-mCh organized into cortical patches and (E) Atg9-3XGFP tethered near cortical ER membranes and (F) the overlay; the numbers indicate smaller Atg9-3XGFP foci at the cortex. The brackets in D and E indicate the region where Atg9-3XGFP membranes are observed near septin patches. The arrowhead indicates an example of a larger Atg9-3XGFP focus. (G) A volume projection of the rapamycin-treated cell in (D–F) rotated (11 degrees) around the X axis; the "1" arrow indicates the position of cortical Atg9-3XGFP and the arrowhead indicates the position of the larger Atg9-3XGFP focus and both correspond to the labels in (F). Scale bar = 5 μm

between septins and Atg9 membranes. We used high-resolution fluorescence microscopy to assess the physical relationship between Atg9 membranes and septins in cells coexpressing Atg9-3XGFP and Cdc3-mCherry. In vegetatively grown cells, Atg9-3XGFP is infrequently found to overlap with septins at the bud neck (Figure 5, A and B; arrow in Figure 5C). After treatment with rapamycin for 6 h, Atg9-3XGFP was observed as foci localized primarily at the cell cortex and surrounded by Cdc3-mCherry patches (Figure 5, D–F). This close physical relationship was true of small and larger Atg9-3XGFP foci (Figure 5, E and F; see the arrowhead). The closely abutted septin patches and Atg9-3XGFP membranes at the cortex are highlighted in volume projections after rotation around the X and Z axes (Figure 5G; additional examples in Supplemental Figure S5; Supplemental Movie 4). It is also clear from the volume view that cortical septins extend past the more limited Atg9-3XGFP signal at the cell cortex. The close proximity of these extended cortical septin patches and Atg9 membranes suggests that septins may directly regulate Atg9 membrane biogenesis or trafficking, known rate-limiting steps in autophagosome formation.

The potential role of cortical septins in regulating Atg9 membranes predicts that loss of cortical septin patches will alter the number and/or distribution of Atg9 membranes. To test this prediction, we analyzed Atg9-3XGFP in wild type and in the two more penetrant septin alleles, *cdc10-1* and *cdc3-6* after the induction of autophagy by rapamycin for 3 h. We quantified the total number of Atg9-3XGFP foci in wild-type and septin-mutant cells grown at 25° and 30°C that coexpress the ER marker, HDEL-dsRed to allow us to define the cell cortex (see *Materials and Methods*). While all strains exhibit an increase in total Atg9-3XGFP foci following rapamycin treatment (unpublished data), an observation that is consistent with previous reports (Yamamoto *et al.*, 2012; and unpublished data), both *cdc10-1* and *cdc3-6* have significantly more Atg9-3XGFP foci compared with wild-type cells at semipermissive temperature (4.8- and 2.5-fold, respectively; Figure 6, A–D). *cdc10-1* also exhibits a modest (1.3-fold), though not significant, increase in Atg9-3XGFP foci even at 25°C, consistent with its more severe septin assembly defect (Figure 6D). The increase in Atg9-3XGFP foci in *cdc10-1* compared with wild-type cells persisted under extended nutrient deprivation (Figure 6H). Importantly, the increase in Atg9-3XGFP foci in wild-type cells peaked at 24 h and decreased with kinetics that parallel the downregulation detected by autophagic flux and PAS formation; in *cdc10-1*, Atg9-3XGFP foci are greater than wild-type cells after 12 h and remain significantly higher throughout the starvation time course (Figure 6, F–H), mirroring the extended during of autophagy.

Interestingly, we observed Atg9-3XGFP foci were more frequently located away from the cell cortex in septin mutants compared with wild-type cells. The number of noncortical Atg9-3XGFP foci increased at nonpermissive temperature and after the induction of autophagy (Figure 6, E and I). The change in Atg9 membrane distribution after the loss of cortical septin patches led us to consider the possibility that septins might act to constrain the diffusion of Atg9 membranes at the cell cortex.

Septins transiently constrain cortical Atg9 diffusion

To test the possibility that cortical septin patches constrain the diffusion of Atg9 membranes tethered to the cortical ER, we recorded time-lapse movies (780 ms/frame; see *Materials and Methods*) of

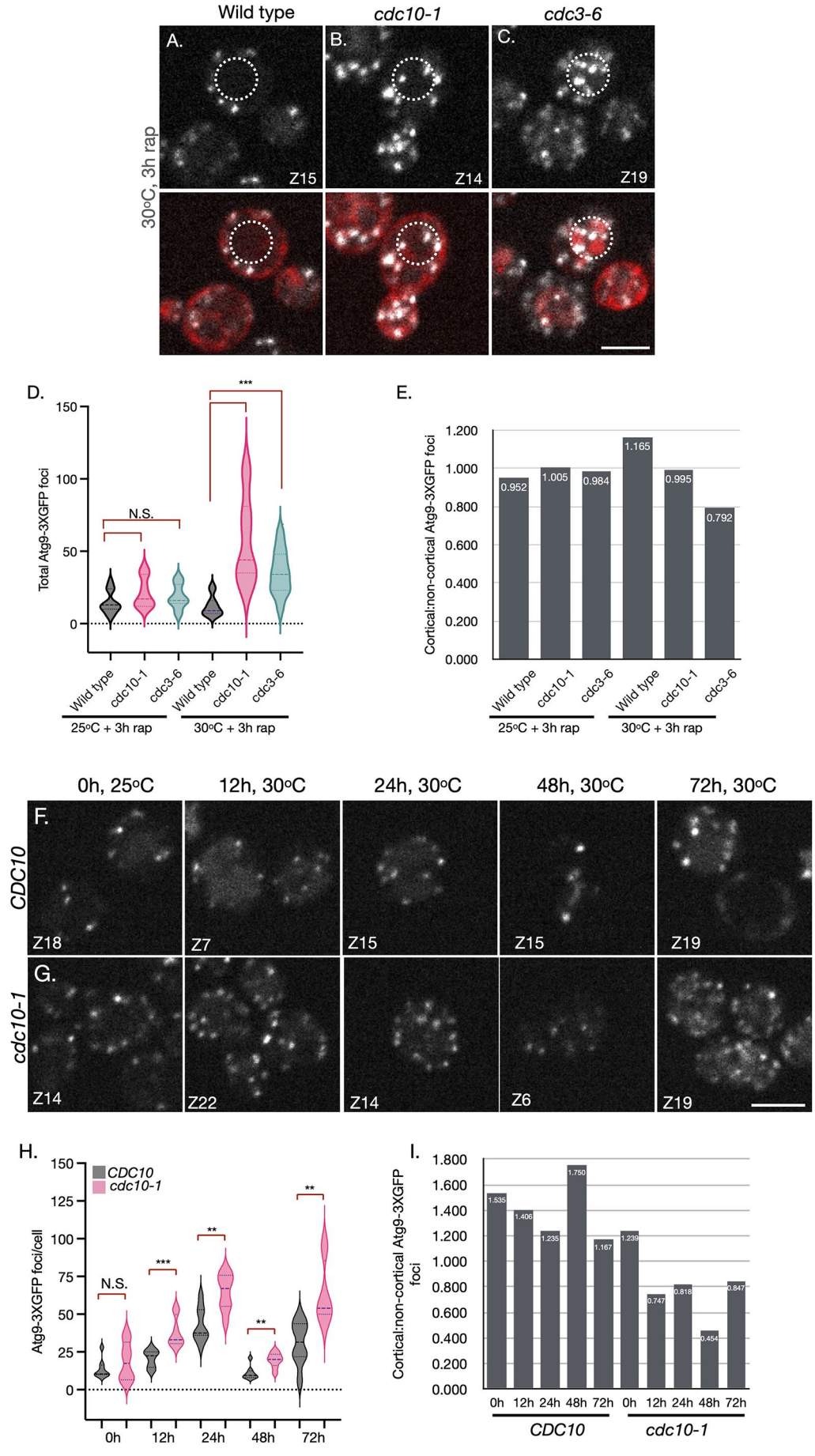
Wild type
cdc10-1
cdc3-6
A.
B.
C.
30°C, 3h rap
Z15
Z14
Z19
D.
Total Atg9-3XGFP foci
150
100
50
0
N.S.
***
Wild type
cdc10-1
cdc3-6
Wild type
cdc10-1
cdc3-6
25°C + 3h rap
30°C + 3h rap
E.
Cortical:non-cortical Atg9-3XGFP foci
1.200
1.000
0.800
0.600
0.400
0.200
0.000
0.952
1.005
0.984
1.165
0.995
0.792
Wild type
cdc10-1
cdc3-6
Wild type
cdc10-1
cdc3-6
25°C + 3h rap
30°C + 3h rap
0h, 25°C
12h, 30°C
24h, 30°C
48h, 30°C
72h, 30°C
F.
CDC10
Z18
Z7
Z15
Z15
Z19
G.
cdc10-1
Z14
Z22
Z14
Z6
Z19
H.
Atg9-3XGFP foci/cell
150
125
100
75
50
25
0
CDC10
cdc10-1
N.S.
***
**
**
**
0h
12h
24h
48h
72h
I.
Cortical:non-cortical Atg9-3XGFP foci
1.800
1.600
1.400
1.200
1.000
0.800
0.600
0.400
0.200
0.000
1.535
1.406
1.235
1.750
1.167
1.239
0.747
0.818
0.454
0.847
0h
12h
24h
48h
72h
0h
12h
24h
48h
72h
CDC10
cdc10-1

wild-type and septin-mutant cells, coexpressing Atg9-3XGFP and HDEL-dsRed and grown at 30°C in the presence of rapamycin for 3 h. HDEL-dsRed provides a marker of the cortex to focus our measurements on ER-tethered, Atg9-3XGFP membranes (see boxes in Figure 7). We used kymographs to measure the duration that cortically localized Atg9-3XGFP foci are positionally constrained (i.e., observed as a continuous line in the kymograph). In wild-type cells, a population of Atg9-3XGFP foci remained constrained for an average time of 142 s (see arrow, Figure 7, A and D). A second population of the cortical Atg9-3XGFP foci exhibited behavior more consistent with random diffusion as suggested by the short, vertical tracks of fluorescence (see yellow arrow in Figure 7A kymograph). The septin mutants, *cdc10-1* or *cdc3-6*, exhibited far fewer examples of constrained behavior as evidenced by the lack of continuous lines in the kymographs and the dramatically reduced average time of constrained behavior (21 s and 31 s for *cdc10-1* and *cdc3-6*, respectively). Importantly, the population of Atg9-3XGFP foci that exhibit constrained diffusion was not observed in vegetatively growing wild-type cells that have septins primarily assembled at the mother-bud neck (i.e., not in patches) and the constrained behavior persisted after long periods of autophagy in a septin-dependent manner (Figure 7, E–G). Together, these results support the hypothesis that cortical septin patches that form after autophagy induction can constrain Atg9 membrane diffusion and thus may contribute to the fine-tuning of the autophagy response.

The septin-dependent transient constraint of Atg9 membranes at the cell cortex following nutrient deprivation is distinct from the more sustained block to diffusion of ER-associated proteins via septins at the bud neck (Takizawa *et al.*, 2000; Seshan *et al.*, 2002; Luedeke *et al.*, 2005; Chao *et al.*, 2014; Sugiyama and Tanaka, 2019). It is possible that the transient constraint is a function of the much smaller assemblies of septins in cortical patches compared with the bud neck. To address this possibility, we examined whether bud neck septins are able to constrain Atg9 membranes tethered to ERES from diffusion across the bud neck. First, we collected time-lapse images from cells coexpressing Atg9-3XGFP and Cdc3-mCh that were grown under nutrient-rich conditions where septins are primarily localized then the bud neck. The slower frame-rate due to coimaging both Atg9-3XGFP and Cdc3-mCh prevented us from observing free diffusion of membranes. However, kymograph analysis along the cell cortex demonstrated an Atg9-3XGFP free zone associated with septins at the bud neck (Supplemental Figure S6, A–C). Imaging only Atg9-3XGFP allowed the measurement of infrequent and short-distance incursions of Atg9-3XGFP into the bud neck area in wild-type cells (Supplemental Figure S6D). In contrast, *cdc10-1* cells similarly analyzed exhibited high frequency incursions that in many cases transited across the bud neck region of the kymograph (Supplemental Figure S6E). This kinetic analysis in nutrient-rich cells is consistent with the ability of septins at the bud neck efficiently block diffusion of Atg9 membranes.

To extend the kinetic measurements of Atg9 membrane diffusion past the bud neck, we used FRAP to examine the ability of septins to block diffusion into the bud as previously shown for a variety of ER-localized proteins (Sugiyama and Tanaka, 2019). Unlike resident ER proteins, Atg9 appears as fluorescent foci that represent membrane vesicles tethered to the ER. Thus, we expect to measure only partial recovery of fluorescence if individual membrane vesicles diffuse across the bud neck. In wild-type cells grown in nutrient-rich conditions, Atg9-3XGFP foci were not observed to enter the daughter bud following photobleaching (Figure 8, A and C, green lines), even when observed using slower frame rates and extended period of times (>4 min, unpublished data). In contrast, *cdc10-1* cells exhibited rapid incursions of Atg9 foci into the daughter bud as soon as 10 s after photobleaching (Figure 8, B and C, red lines). We conclude that septins at the bud neck fully block the diffusion of Atg9 membranes tether to ERES and that the transient constraint of diffusion during nutrient starvation is due to smaller assemblies of septins in cortical patches. Together, these findings support the role of septins in limiting the diffusion of Atg9 membranes at the cortex as a possible mechanism for modulating autophagy.

DISCUSSION

We have shown that during autophagy induction septins reorganize primarily to patches distributed along the cell cortex. Cortical septin patches surround Atg9 membranes tethered to the cortical ER where they act to constrain the free diffusion of Atg9 membranes tethered to ERES. In the absence of cortical septin patches, Atg9 membrane diffusion is less constrained at the cortex, a behavior that correlates with an increase in the magnitude and duration of autophagosome formation and autophagic flux (see model, Figure 9). We propose that septins act to modulate the autophagy response, preventing extended Atg9-dependent assembly of autophagosomes during prolonged nutritional stress.

Septin localization in cortical patches occurs rapidly after the induction of autophagy, and though the initial patches are low intensity, they mature over time increasing in intensity and growing in length into bar-like structures that interdigitate with cortical ER. Though septin cortical patches initiate before disassembly of septin rings as cells exit mitosis, the full maturation of septin patches coincides with the disassembly of septin rings at the bud neck, as cells enter a prolonged G1 due to nutrient deprivation. Six to twelve hours after induction of autophagy, septins are clearly observed

FIGURE 6: Atg9-3XGFP foci increase in number and become less enriched at the cortex in septin mutants. (A) Wild-type, (B) *cdc10-1*, and (C) *cdc3-6* cells were grown to log phase and treated with rapamycin for 3 h. Cells were imaged and individual Z-slices in the middle of the cell are displayed for Atg9-3XGFP (top panels) and overlaid with HDEL-dsRed (bottom panels). Dashed circles indicate the demarcation between cortical Atg9 membranes and noncortical membranes (see *Materials and Methods*). (D) The total number of Atg9-3XGFP foci were quantified using the three-dimensional-Focipicker plugin in Image J (see *Materials and Methods*) and the data is presented in a violin plot for cells treated with rapamycin for 3 h and grown at either permissive temperature (25°C) or semipermissive temperature (30°C). Darker dashed lines represent the median seconds constrained and the lighter dashed lines represent the position of quartile values. The *p* values from a Welch unpaired *t* test are represented as follows: NS - $p > 0.05$; * - $p < 0.05$; ** - $p < 0.005$; *** - $p < 0.001$. (E) The ratio of cortical Atg9-3XGFP foci:noncortical foci was determined for the data described in (D). (F) Wild-type and (G) *cdc10-1* cells were grown to log phase (0 h time-point) and switched to nutrient-limiting conditions for the indicated time points and representative images from single Z-slices are presented. (H) The total number of Atg9-3XGFP foci was determined and analyzed as in (D) for wild-type and *cdc10-1* cells. (I) The ratio of cortical Atg9-3XGFP foci:noncortical foci was determined for the cells described in (F) and (G). Scale bar = 5 μm

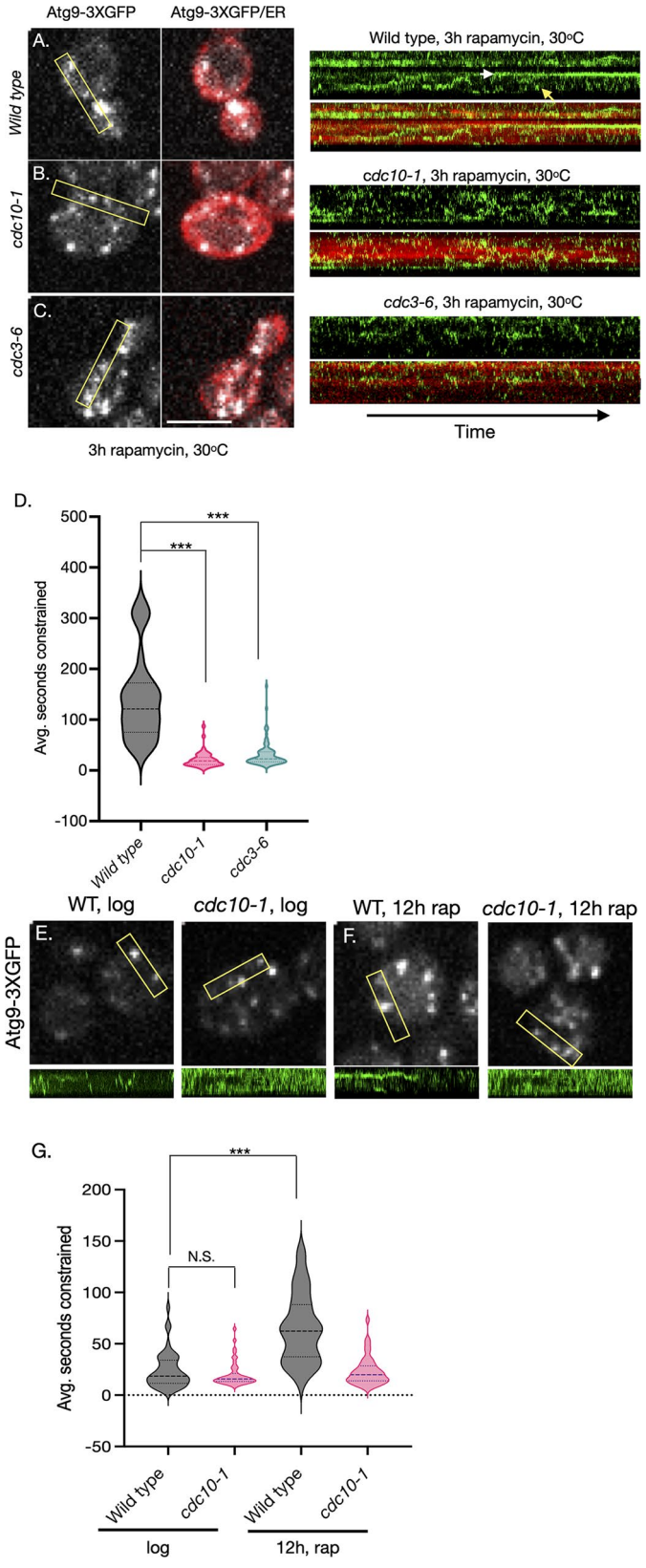

FIGURE 7: Time-lapse movies of Atg9-3XGFP diffusion in wild-type and septin mutants. (A–C) The indicated strains were grown to log phase and treated with rapamycin for 3 h at 30°C. Atg9-3XGFP and HDEL-dsRed were imagined in a single Z-slice at 780 ms/frame. Kymograph analysis was performed selectively on Atg9-3XGFP and HDEL-dsRed at the cortex of cells (see yellow boxes; 10–15 cells for each strain). Kymographs are displayed to show Atg9-3XGFP (green) and the overlay with HDEL-dsRed (red). Time 0 is at the left end of the kymograph and a total of 500 frames (390 s) are represented. The white arrow in the kymograph associated with (A) indicates a Atg9-3XGFP foci that begins a period of transient constraint (solid kymograph line to the right of the arrow). The yellow arrow indicates a Atg9-3XGFP foci that moves rapidly and randomly at the cortex. (D) The continuous lines for wild-type, *cdc10-1*, and *cdc3-6* were measured and converted to seconds; the average time for all lines in multiple cells is graphed in a violin plot as the average time constrained. Darker dashed lines represent the median seconds constrained and the lighter dashed lines represent the position of quartile values. Time-lapse images were collected for wild-type and *cdc10-1* cells E) grown in nutrient-rich conditions or (F) after 12 h of rapamycin treatment and (G) average duration of constrained Atg9-3XGFP foci were calculated and graphed as in (D). The *p* values from a Welch unpaired *t* test are represented as follows: NS - $p > 0.05$; * - $p < 0.05$; ** - $p < 0.005$; *** - $p < 0.001$.

surrounding Atg9 membranes at the cortex (see Figure 6). The gradual maturation of these septin structures suggests that their ability to constrain cortical Atg9 membrane increases during nutrient deprivation. This conclusion is consistent our finding that Atg9 membrane diffusion is not constrained at the cell cortex outside of the bud neck in vegetatively growing cells (Figures 7 and 8). Although we observe a small fraction of cells with septins associated with PAS, as previously reported (Barve *et al.*, 2018b; Figure 1; Supplemental Figure S1), we propose that this represents infrequent de novo assembly of septins on negatively charged membranes associated with a subset of forming autophagosomes, or rare trafficking events perhaps from endosomal membranes (Barve *et al.*, 2018a). Regardless of their origin, our analysis demonstrates that septins at PAS are neither required for PAS formation nor for autophagy.

The relationship between the disassembly of septins at the bud neck and the formation of cortical patches appears to be complex. We know that under nutrient deprivation conditions assembly of septin patches is not initially dependent on disassembly of septin filaments at the bud neck. We observe that septin patches form at early time points after autophagy induction before bud neck septin disassembly. In addition, septin disassembly occurs in multiple steps. Septin filaments remain stable after rapamycin treatment until cells exit from mitosis, where instead of disassembling and reforming at the incipient bud-site, large assemblies of septin filaments are observed to migrate along the cell cortex (see Supplemental Movie 2). Nearly coincident with this dramatic rearrangement we observe low intensity septin patches at the cell cortex (1440 ms time point; Supplemental Figure S2A), implying that a bud neck–independent pool of septin building blocks is initially used after induction of autophagy. The large assemblies of septins eventually completely disassemble between 6 and 12 h after autophagy induction. During this time cortical septin patches mature gaining in both the amount of septin subunits and in size, raising the possibility that disassembling septin filaments from the bud neck contribute to the maturation of septin patches at the cortex. Given septin affinity for negatively charged phospholipids (Bertin *et al.*, 2008, 2010, 2012), it is interesting to speculate that changes in membrane lipid modifications are driving both the assembly of cortical patches as well as the disassembly of septins at the site of cell division. The reports of septins overlapping with endosomes under starvation conditions suggests an additional mode of trafficking septins, though this association is limited to a subset of cortical septin patches (Barve *et al.*, 2018a). Recent studies have suggested that ER stress signals

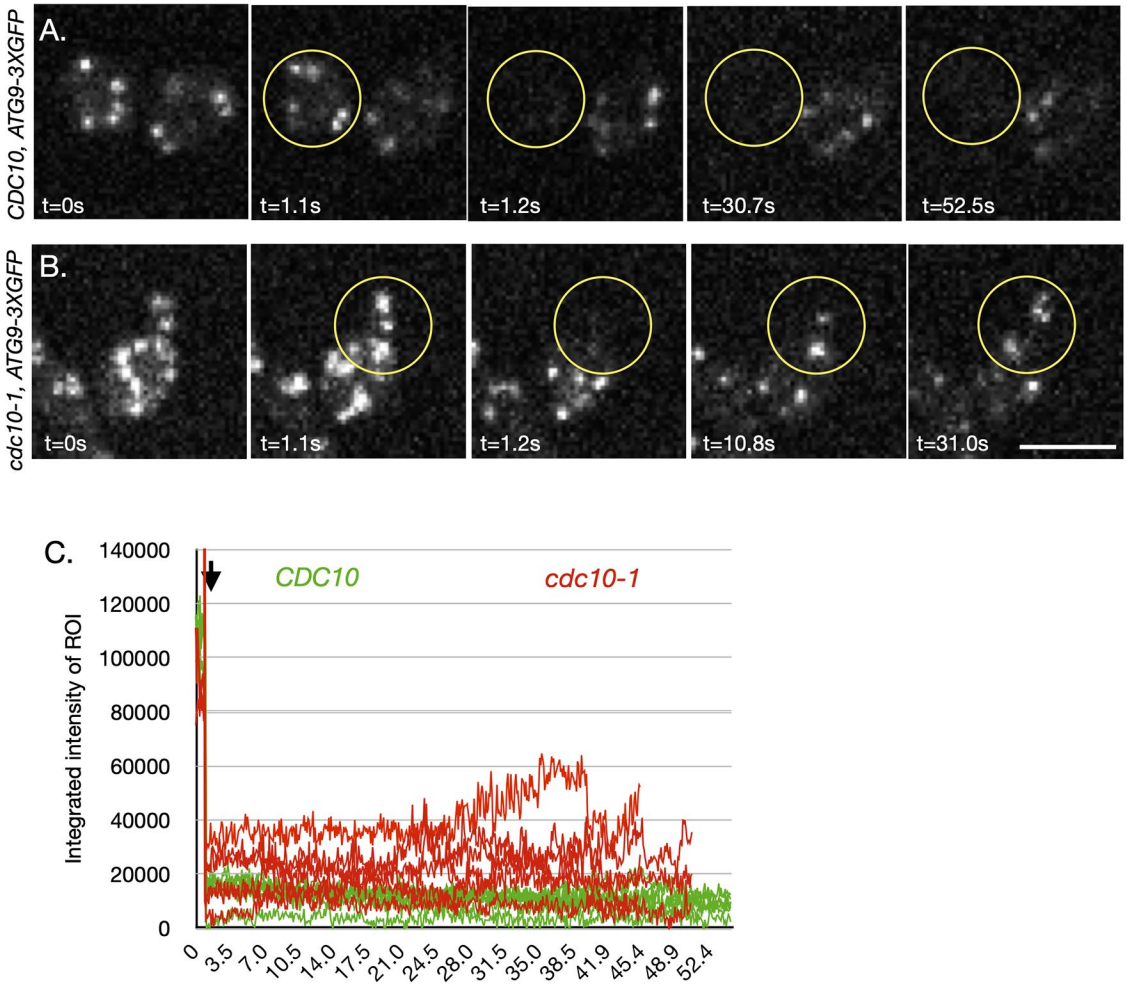

FIGURE 8: FRAP of Atg9-3XGFP membrane diffusion at the bud neck in vegetatively growing cells. Wild-type cells (A) or *cdc10-1* cells (B) expressing Atg9-3XGFP were grown at 30°C under nutrient-rich conditions. Cells were imaged at ~80 ms increments in a single Z slice for 500 frames after photobleaching (see *Materials and Methods*) and representative images from the time lapse are shown before photobleaching (t = 0s and t = 1.1s), immediately after the photobleach (*t* = 1.2 s) and during the recovery period (*t* > 1.2s). The circles represent the position of the photobleaching. (C) The integrated intensities were measured using the ROI represented by the circles. The time point of the photobleach is indicated by the arrow. Signal from wild-type cells (green) is compared with signal from *cdc10-1* cells (red) for similar time periods.

through the Slt2 stress kinase to cause an analogous change in septin organization as they transition from the bud neck to cytokinetic remnants, allowing cells to efficiently rebud after ER homeostasis is restored (Babour *et al.*, 2010; Chao *et al.*, 2019). The connection between septin organization and the return to homeostasis after ER stress or nutrient deprivation–induced autophagy (another form a cell stress) is suggestive of a broader role for septins in maintaining homeostasis at the cortical ER–plasma membrane interface. The precise modifications downstream of Slt2 that result in septin reorganization, and whether these same pathways are active during induction of bulk autophagy, are fascinating questions that remain to be explored.

Mechanisms underlying the modulation and fine-tuning of the autophagy response are not well understood. Reports have described a transcriptional repressor network that combines with post-transcriptional activities to keep autophagy genes minimally expressed in nutrient-rich conditions (Delorme-Axford and Klionsky, 2018; Delorme-Axford *et al.*, 2018). One hallmark of loss of these repressor activities is that autophagy is elevated in nutrient-rich conditions. Septin mutants show no change in autophagic flux or other autophagy markers in nutrient-rich conditions compared with wild-type cells, arguing against their role in the transcriptional and post-transcriptional regulatory networks that repress autophagy. One possibility is that while repression of autophagy is normal, there is a more robust amplification of ATG gene expression in septin mutants after induction of autophagy. However, GFP-Atg8 expression from its native promoter is not elevated in septin mutants (e.g., *cdc10-1* expresses less or equal levels of GFP-Atg8 over a time course of nutrient deprivation; Supplemental Figure S3C). Deletion of the *PHO23* transcriptional repressor targeting subunit increases levels of Atg9 and results in more autophagic flux relative to wild-type within 2–3 h of switch to nutrient deprivation conditions (Jin and Klionsky, 2014; Jin *et al.*, 2014). Though we see a faster rate of flux in septin mutants (Supplemental Figure 3B), we do not see overall higher levels of flux compared with wild-type cells. The increase in Atg9 membranes (i.e, Atg9 foci) may result from an alteration in the rate of either anterograde or retrograde trafficking of Atg9 membranes near the cortex (see model, Figure 9). Our results do not

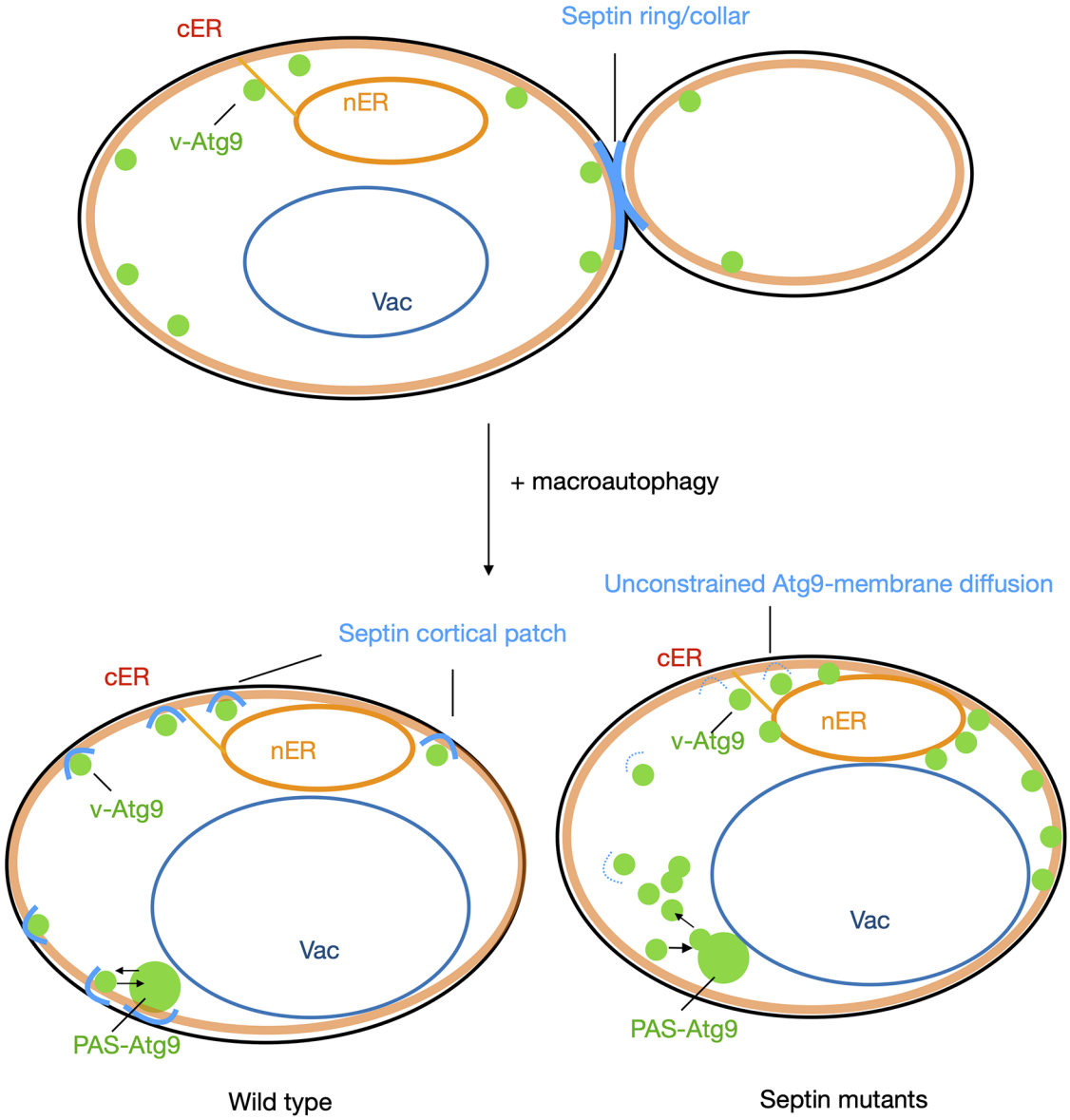

FIGURE 9: A model for septin-mediated Atg9 membrane diffusion regulation during prolonged nutrient deprivation: In vegetatively growing cells, septins (blue) form rings or collars at the bud neck; Atg9 membranes (green) are found primarily at the cortical ER (cER), presumably associated with ERES and are unable to diffuse past the septin ring/collar. After induction of autophagy, septins assemble into cortical patches at the junction between the plasma membrane (black line) and the cER where the transiently constrain Atg9-positive membrane diffusion thus limiting access to PAS and autophagosome biogenesis. Septin patches near PAS may also contribute to the efficiency of retrograde transport of Atg9-positive membranes. In septin mutants, cortical patches fail to form allowing less constrained diffusion of Atg9-positive membranes, increased access to PAS, and extended autophagosome biogenesis.

distinguish between these two possibilities, but they do suggest that an increase in Atg9 vesicles that persists during prolonged nutrient deprivation is connected to the persistence of autophagic flux.

The physical proximity of septin patches to cortically tethered Atg9 membranes and the results from rapid acquisition imaging of Atg9-3XGFP membrane diffusion properties argue that septins constrain the free diffusion of Atg9 membranes both at cortical patches after nutrient deprivation and at the bud neck during vegetative growth. The ability of cortical patches to only transiently constrain diffusion compared with the more complete block at the bud neck might reflect a difference in the biochemical makeup of the two septin assemblies or in the relative amount of septin filaments in each region. There are clearly less septin subunits in patches compared with the bud neck (~10-fold more fluorescence signal at the bud neck than patches; unpublished measurements). The proposed ability of septins to partition ER–plasma membrane attachment sites might be dependent on the large number of assembled septin filaments at the bud neck (Sugiyama and Tanaka, 2019). Thus, septins at cortical patches might only form transient partitions. However, our high-resolution imaging of ER membranes does not reveal the partitioning of ER in starved cells compared with vegetatively grown cells (i.e., plus and minus cortical septin patches, respectively). Alternatively, it is also possible that the transient block to diffusion works by some other mechanism than septin-dependent plasma membrane–ER partitioning. Interestingly, a similar septin-dependent

transient block to the diffusion of the GluA2 subunit of the AMPA-type glutamate receptor has been reported in the plasma membrane of neuronal dendritic spines, where septins form more patch-like structures at the base of the spine (Ewers *et al.*, 2014). It is interesting to speculate that septin filaments can be regulated to create a range of membrane partitions to tune membrane protein diffusion depending on the cellular context.

In conclusion, our studies have provided novel insight into the role of septins during autophagy and into the mechanisms that fit into a larger homeostatic feedback pathway to limit autophagy spatially and temporally under a variety of cell stress conditions.

MATERIALS AND METHODS

Request a protocol through *Bio-protocol*.

Yeast growth, treatments, strain construction, and plasmids

Strains were grown in synthetic medium (0.7% [wt/vol] yeast nitrogen base, 2% [wt/vol] glucose) at 30°C supplemented with necessary amino acids for plasmid retention or in complete media. Septin mutants were grown at permissive temperature (25°C) and then shifted to 30 or 37°C for the indicated times. For nitrogen starvation, yeast were grown to mid-log phase in rich media then shifted to nitrogen starvation media (0.17% [wt/vol] yeast nitrogen base without amino acids or ammonium sulfate, 2% [wt/vol] glucose, and 0.006% [wt/vol] adenine). For rapamycin treatment, cells were grown to mid log phase then rapamycin (Peptides International, IRA-3884-PI) dissolved in dimethyl sulfoxide was added to achieve a working concentration of 200 ng/mL.

For vacuolar staining with the FM 4-64 dye, cells were centrifuged for 1 min at 15,000 × g at room temperature before treatment. Cells were resuspended in 500 µl of medium with 8 µM FM 4-64 (Life Technologies, Molecular Probes (F34653), Eugene, OR) and incubated for at least 30 min before washing cells with medium alone and treating as described for at least 90 min to allow the dye to enrich in the vacuole.

Strains (listed in Supplemental Table S1) used in this study were derived from S288C with the exception of KSC3880 which derives from W303a. Temperature-sensitive septin mutants were a kind gift from the Pringle lab. Transformations were done with the lithium acetate protocol as published (Gietz and Woods, 2002). PCR-based targeted homology was used to delete the entire open-reading frame of genes with their noted cassettes. Atg9-3xGFP was a gift from Nunnari lab and the *atg7*Δ stain from the Powers lab (Graef *et al.*, 2013; Vlahakis *et al.*, 2017); these loci were moved into strains using PCR-mediated homologous recombination methods. All strains were confirmed using PCR screening and DNA sequencing when necessary. Plasmids used in these studies are listed in Supplemental Table SII (see Supplemental Data).

Fluorescence Microscopy

For microscopy experiments, cells were treated as described and concentrated for mounting on 4% low melting point agarose pads (Invitrogen, 15517-022), resuspended in the appropriate medium, sealed with an equal ratio of vaseline, Lanolin (Sigma Aldrich, L7387) and Paraffin (Fisher, 8007-74-2). Cells were imaged using a 3i (Intelligent Imaging Innovations, Denver CO), spinning disk confocal microscope and a 63X (NA 1.4) objective using the Slidebook software. Fixed time point images were collected using a Hamamatsu qCMOS (1792 × 1304 effective pixel area) camera. Rapid acquisition time-lapse images were collected using a Photometrics Evolve 16 EMCCD camera (512 × 512 effective pixel area). For Atg9-3xGFP time series (500 frames), frames were collected with a gain setting of two and an amplification setting of 800 with no time delay between frames. Actual time increments are reported in the text. FRAP experiments were carried out using the 488-nm laser line and the Slidebook FRAP module. Well separated cells with medium- to large-sized daughter buds were selected and the photobleach ROI positioned toward the edge of the daughter to avoid incidental photobleaching of the mother. Images were acquired at ~80 ms increments for 500 frames after photobleaching.

For long-term imaging of septin GFP fusions under starvation conditions, we used the 3i lattice light-sheet microscope outfitted with a 63X (NA 1.4) objective. Briefly, cells were grown and treated as described and then attached to Concanavalin A (ConA) coated coverslips before imaging. Coverslips were prepared by cleaning first in 70 and then 100% ethanol and allowed to dry completely. Coverslips were incubated with 0.25 mg/ml ConA for 90 min at room temperature and allowed to dry before applying cells. Images were collected at 10ms increments using a Hamamatsu, Orca-Flash 4.0 (512 × 512 pixel area) camera for the durations indicated. Images were deconvolved as described below.

Image processing and analysis

Multilayer TIFF images were prepared using Image J (ImageJ2, version 2.9.0/1.53t downloaded from https://fiji.sc/). Where noted, TIFF images were processed using deconvolution software (Huygens Software, SVI NL). PSF files for deconvolution were generated using Tetraspeck (Molecular Probes, Eugene OR) 100 nm fluorescent beads under identical conditions used to image living yeast cells. Processing was also carried out using the Huygens software theoretical PSF calculations for some images. Deconvolved images were processed as above using ImageJ. Volume projections of cells were prepared using the Volume Viewer 2.01 plugin in Image J (https://imagej.nih.gov/ij/plugins/volume-viewer.html) using a tricubic smooth interpolation mode. The degrees of rotation around the X-axes are indicated in the figure legends.

Quantification of GFP-Atg8 structures are described in the text. Briefly, multiple fields of cells ($n > 250$ cells for all points) were analyzed for the presence of PAS structures, the frequency of PAS/cell and the presence of GFP signal in the vacuole, using either DIC images or coimaging with BFP-Pho8 or FM 4-64 treated cells to identify the vacuole-specific fluorescence signal. Quantification of Atg9-3X-GFP foci was performed using the FociPicker3D plugin for ImageJ (https://imagej.nih.gov/ij/plugins/foci-picker3d/index.html) and multi-Z TIFFs with general settings adjusted to identify >95% of foci in a given Z-stack (MinL = 100–120, MinPixel = 75–95, tolerance = 45). Settings were verified by hand-counting foci in a limited number of cells. Cortical and noncortical Atg9 foci were classified based on their position relative to the boundary of the HDEL-dsRed cortical ER. Foci distal to the ER boundary were classified as cortical and foci proximal were classified as noncortical foci. The mobility of Atg9-3X-GFP foci was measured by creating a kymograph using an ROI fit to the cortical region indicated in the images. The resulting kymograph was converted to seconds/pixel and the seconds foci were constrained was determined by measuring the length of observable fluorescent lines. For all quantifications, sample number is listed in the figure legend and where appropriate. Violin plots and statistical analyses were created using Prism Graphpad (v10.0, www.graphpad.com/). Unless otherwise noted, all experimental results are from at least three independent experiments. For data with normal distributions, two-sided Student's *t* tests or one-way analysis of variance (ANOVA) analyses were carried out as indicated. Welch's correction for unequal variances was used with *t* tests comparing

two groups with large differences in SD. We concluded statistical significance for p values ≤ 0.05 and details can be found in either in figures or figure legends.

Cell Viability and Death Assays

Cells were grown to mid-log phase in rich media then shifted to nitrogen starvation media and incubated at the indicated times and temperatures. Cell densities were determined by counting in a hemacytometer and 500 cells were then plated in triplicate on yeast extract peptone dextrose (YPD) plates (1% yeast extract, 2% peptone, and 2% glucose) and colonies were counted after 24–48 h of growth. Colony counts were averaged between triplicates and the percent viability was scored as colonies formed relative to wild-type in nutrient-rich medium.

To determine the rate of cell death, cells were grown to mid-log phase in rich media then shifted to nitrogen starvation media and incubated for the described times and growth temperatures. Cell death assays using phloxin B (Millipore, 115926) were performed as previously described (Suzuki *et al.*, 2011).

Cell lysates, Western blotting, and analysis

Cell pellets consisting of 10×10^7 cells were collected then incubated in 1.85N NaOH and 7.84% β-mercaptoethanol on ice for 10 mins then 50% Trichloroacetic acid was added and incubated on ice for 10 mins. The pellet was centrifuged at 14,000 × *g* at 4°C for 10 mins and washed in 100% acetone then resuspended in sample buffer (500 mM Tris, 6.5% sodium dodecyl sulfate (SDS), 100 mM dithiothreitol, 12% Glycerol) boiled at 95°C, recentrifuged as above; the supernatant was diluted 1:1 in loading buffer (125 mM Tris pH 6.8, 2% SDS, 10% Glycerol) before loading onto a 10% SDS–PAGE gel. Samples were transferred overnight onto a nitrocellulose membrane using a tank transfer system in (buffer). Membranes were blocked for 1 h at 25°C (2% nonfat powdered milk in Tris-buffered saline (TBS; 20 mM Tris base, pH 7.5, 150 mM NaCl)) and then incubated with anti-GFP N86/8 mouse monoclonal antibody (1:4000; UC Davis/NeuroMab Facility, 73–131) and rabbit anti-Sgt1 as a loading control (1:4000; diluted in 2% gelatin in phosphate-buffered saline) at 25°C for 3–6 h. Membranes were then incubated with secondary antimouse and antirabbit fluorescent antibodies (1:10000; LiCor, 926-68071, and 926-32212; diluted in 2% gelatin in TBS + 0.2% Tween 20), incubated for 1 h at 25°C and then scanned using the LiCor Odyssey Imager. Fluorescent signals were quantified using the ImageJ software.

Autophagic flux was measured as described (Klionsky *et al.*, 2021). Briefly, bands corresponding to full length GFP-Atg8 and the GFP fragment were quantified using the same size ROI in ImageJ and background signal was subtracted; loading variation was corrected using Sgt1 signal (unpublished data) and the GFP: GFP-Atg8 ratio was calculated for each time point. To control for equal sample loading, all Western blots were incubated with a Sgt1 antibody (Catlett and Kaplan, 2006) or a PGK antibody (Molecular Probes, A-6457, Eugene OR) and where relevant used to control for loading. At least three experiments were included for each data point in Figure 3D.

ACKNOWLEDGMENTS

The authors would like to acknowledge Jonathan Mendes and the 2016 MCB140L lab class for noting the change in septins in starved cells. We also want to acknowledge the technical assistance of Thomas Wilkop in the MCB Light Microscopy Core. Finally, we thank Ted Powers for comments on the work during its progress.

REFERENCES

Babour A, Bicknell AA, Tourtellotte J, Niwa M (2010). A surveillance pathway monitors the fitness of the endoplasmic reticulum to control its inheritance. Cell 142, 256–269.

Barve G, Sanyal P, Manjithaya R (2018a). Septin localization and function during autophagy. Curr Genet 64, 1037–1041.

Barve G, Sridhar S, Aher A, Sahani MH, Chinchwadkar S, Singh S, Lakshmeesha KN, McMurray MA, Manjithaya R (2018b). Septins are involved at the early stages of macroautophagy in S. cerevisiae. Journal Cell Sci 131, jcs209098.

Bertin A, McMurray MA, Grob P, Park S-S, Garcia G, Patanwala I, Ng H-L, Alber T, Thorner J, Nogales E (2008). Saccharomyces cerevisiae septins: supramolecular organization of heterooligomers and the mechanism of filament assembly. Proc Natl Acad Sci USA 105, 8274–8279.

Bertin A, McMurray MA, Thai L, Garcia G, Votin V, Grob P, Allyn T, Thorner J, Nogales E (2010). Phosphatidylinositol-4,5-bisphosphate promotes budding yeast septin filament assembly and organization. J Mol Biol 404, 711–731.

Bertin A, McMurray MA, Pierson J, Thai L, McDonald KL, Zehr EA, Garcia G, Peters P, Thorner J, Nogales E (2012). Three-dimensional ultrastructure of the septin filament network in Saccharomyces cerevisiae. Mol Biol Cell 23, 423–432.

Catlett MG, Kaplan KB (2006). Sgt1p Is a Unique Co-chaperone That Acts as a Client Adaptor to Link Hsp90 to Skp1p*. J Biol Chem 281, 33739–33748.

Cebollero E, Reggiori F (2009). Regulation of autophagy in yeast Saccharomyces cerevisiae. Biochim Biophys Acta 1793, 1413–1421.

Chao JT, Piña F, Onishi M, Cohen Y, Lai Y-S, Schuldiner M, Niwa M (2019). Transfer of the septin ring to cytokinetic remnants in ER stress directs age-sensitive cell-cycle re-entry. Dev Cell 51, 173–191.e5.

Chao JT, Wong AKO, Tavassoli S, Young BP, Chruscicki A, Fang NN, Howe LJ, Mayor T, Foster LJ, Loewen CJR (2014). Polarization of the Endoplasmic reticulum by ER-septin tethering. Cell 158, 620–632.

Chen Y, Gibson SB (2021). Three dimensions of autophagy in regulating tumor growth: cell survival/death, cell proliferation, and tumor dormancy. Biochim Biophys Acta Mol Basis Dis 1867, 166265.

Delorme-Axford E, Klionsky DJ (2018). Transcriptional and post-transcriptional regulation of autophagy in the yeast Saccharomyces cerevisiae. J Biol Chem 293, 5396–5403.

Delorme-Axford E, Abernathy E, Lennemann NJ, Bernard A, Ariosa A, Coyne CB, Kirkegaard K, Klionsky DJ (2018). The exoribonuclease Xrn1 is a post-transcriptional negative regulator of autophagy. Autophagy 14, 1–47.

Ewers H, Tada T, Petersen JD, Racz B, Sheng M, Choquet D (2014). A septin-dependent diffusion barrier at dendritic spine necks. PLoS One 9, e113916.

Feng Y, He D, Yao Z, Klionsky DJ (2014). The machinery of macroautophagy. Cell Res 24, 24–41.

Gietz R, Woods R (2002). Transformation of yeast by lithium acetate/single-stranded carrier DNA/polyethylene glycol method. Methods Enzymol 350, 87–96.

Graef M, Friedman JR, Graham C, Babu M, Nunnari J (2013). ER exit sites are physical and functional core autophagosome biogenesis components. Mol Biol Cell 24, 2918–2931.

Jin M, He D, Backues SK, Freeberg MA, Liu X, Kim JK, Klionsky DJ (2014). Transcriptional regulation by Pho23 modulates the frequency of autophagosome formation. Curr Biol 24, 1314–1322.

Jin M, Klionsky DJ (2014). Transcriptional regulation of ATG9 by the Pho23-Rpd3 complex modulates the frequency of autophagosome formation. Autophagy 10, 1681–1682.

Klionsky DJ, *et al.* (2003). A Unified Nomenclature for yeast autophagy-related genes. Dev Cell 5, 539–545.

Klionsky DJ, *et al.* (2021). Guidelines for the use and interpretation of assays for monitoring autophagy (4th edition) 1. Autophagy 17, 1–382.

Komatsu M, *et al.* (2005). Impairment of starvation-induced and constitutive autophagy in Atg7-deficient mice. J Cell Biol 169, 425–434.

Lei Y, Klionsky DJ (2021). The emerging roles of autophagy in human diseases. Biomed 9, 1651.

Lobato-Márquez D, Krokowski S, Sirianni A, Larrouy-Maumus G, Mostowy S (2019). A requirement for septins and the autophagy receptor p62 in the proliferation of intracellular Shigella. Cytoskeleton 76, 163–172.

Luedeke C, Frei SB, Sbalzarini I, Schwarz H, Spang A, Barral Y (2005). Septin-dependent compartmentalization of the endoplasmic reticulum during yeast polarized growth. J Cell Biol 169, 897–908.

Marquardt J, Chen X, Bi E (2021). Septin assembly and remodeling at the cell division site during the cell cycle. Front Cell Dev Biol 9, 793920.
Matoba K, *et al*. (2020). Atg9 is a lipid scramblase that mediates autophagosomal membrane expansion. Nat Struct Mol Biol 27, 1185–1193.
McMurray MA, Thorner J (2009). Septins: molecular partitioning and the generation of cellular asymmetry. Cell Div 4, 18.
Meng T, Lin S, Zhuang H, Huang H, He Z, Hu Y, Gong Q, Feng D (2019). Recent progress in the role of autophagy in neurological diseases. Cell Stress 3, 141–161.
Mizushima N, Levine B, Cuervo AM, Klionsky DJ (2008). Autophagy fights disease through cellular self-digestion. Nature 451, 1069–1075.
Noda T, Kim J, Huang WP, Baba M, Tokunaga C, Ohsumi Y, Klionsky DJ (2000). Apg9p/Cvt7p is an integral membrane protein required for transport vesicle formation in the Cvt and autophagy pathways. J Cell Biol 148, 465–480.
Noda T, Ohsumi Y (1998). Tor, a phosphatidylinositol kinase homologue, controls autophagy in yeast. J Biol Chem 273, 3963–3966.
Orii M, Tsuji T, Ogasawara Y, Fujimoto T (2021). Transmembrane phospholipid translocation mediated by Atg9 is involved in autophagosome formation. J Cell Biol 220, e202009194.
Reggiori F, Tucker KA, Stromhaug PE, Klionsky DJ (2004). The Atg1-Atg13 complex regulates Atg9 and Atg23 retrieval transport from the pre-autophagosomal structure. Dev Cell 6, 79–90.
Robertin S, Mostowy S (2020). The history of septin biology and bacterial infection. Cell Microbiol 22, e13173.
Russo G, Krauss M (2021). Septin remodeling during mammalian cytokinesis. Front Cell Dev Biol 9, 768309.
Seshan A, Bardin AJ, Amon A (2002). Control of Lte1 localization by cell polarity determinants and Cdc14. Curr Biol 12, 2098–2110.
Spiliotis ET, Gladfelter AS (2012). Spatial guidance of cell asymmetry: septin GTPases show the way. Traffic 13, 195–203.
Sugiyama S, Tanaka M (2019). Distinct segregation patterns of yeast cell-peripheral proteins uncovered by a method for protein segregatome analysis. Proc Natl Acad Sci USA 116, 8909–8918.
Suzuki SW, Onodera J, Ohsumi Y (2011). Starvation induced cell death in autophagy-defective yeast mutants is caused by mitochondria dysfunction. PLoS One 6, e17412.
Takizawa PA, DeRisi JL, Wilhelm JE, Vale R-D (2000). Plasma membrane compartmentalization in yeast by messenger RNA transport and a septin diffusion barrier. Science 290, 341–344.
Tsukada M, Ohsumi Y (1993). Isolation and characterization of autophagy-defective mutants of Saccharomyces cerevisiae. FEBS Lett 333, 169–174.
Vlahakis A, Muniozguren NL, Powers T (2017). Stress-response transcription factors Msn2 and Msn4 couple TORC2-Ypk1 signaling and mitochondrial respiration to ATG8 gene expression and autophagy. Autophagy 13, 1804–1812.
Woods BL, Gladfelter AS (2021). The state of the septin cytoskeleton from assembly to function. Curr Opin Cell Biol 68, 105–112.
Xie Z, Nair U, Klionsky DJ (2008). Atg8 controls phagophore expansion during autophagosome formation. Mol Biol Cell 19, 3290–3298.
Yamamoto H, Kakuta S, Watanabe TM, Kitamura A, Sekito T, Kondo-Kakuta C, Ichikawa R, Kinjo M, Ohsumi Y (2012). Atg9 vesicles are an important membrane source during early steps of autophagosome formation. J Cell Biol 198, 219–233.